Bull Volcanol (2005) 67:72–91
DOI 10.1007/s00445-004-0369-3

RESEARCH ARTICLE

**Emmanuelle Cecchi · Benjamin van Wyk de Vries ·
Jean-Marc Lavest**

Flank spreading and collapse of weak-cored volcanoes

Received: 17 July 2003 / Accepted: 19 April 2004 / Published online: 18 August 2004

Abstract Volcanoes subjected to hydrothermal activity develop weak cores as a result of alteration and due to elevated pore pressures. Edifices constructed at the angle of repose of volcanoclastics, or at even more gentle slopes, respond to internal weakening by initially deforming slowly, but may then collapse catastrophically. Such a process has so far been described for only a few volcanoes, such as Casita, Nicaragua; however, the conditions for flank spreading are widespread and many, if not most volcanoes should suffer some alteration-related flank spreading. We provide analogue models that characterise the structure — surface deformation fields and internal structures — of a spreading flank. Deformation creates a characteristic concave-convex-concave flank profile producing structures such as basal thrusts, summit normal faults, grabens and strike-slip relay faults. Three deformation regimes are found: a 'pit collapse' regime is associated with very small volumes of ductile material located far from the edifice surface. This would not appear in nature, as time for deformation is greater than the lifetime of a volcano, unless very low rock viscosities are present. The other two regimes are flank spreading regimes, one symmetric and one asymmetric. The latter is the most common, as most volcanic structures are asymmetrical in form and in distribution of physical properties. The deformation is controlled by altered region dimensions, volume and position relative to the edifice, and to a lesser extent by its shape. As the flanks spread, landslides are created, initially on the steepened portion, but also from fault scarps. Major flank collapse may occur leading to explosive hydrothermal decompression and to a debris avalanche rich in hydrothermally altered material. We provide several new examples of volcanoes that have structures and morphologies compatible with flank spreading. We suggest that it is a common feature, important in the tectonics and hazards of many volcanoes.

Keywords Gravitational deformation · Analogue modelling · Hydrothermal alteration · Edifice weakening · Flank spreading · Volcano instability · Collapse

Introduction

The 1998 landslide and lahar of Casita volcano, Nicaragua, prompted us to re-examine the edifice's morphology and structure, leading to the discovery of flank spreading caused by hydrothermal alteration (van Wyk de Vries et al. 2000). This paper proposed that volcanic edifices are initially built at the angle of repose of scoria, pyroclastics, and by lava accumulation, leading to a stable construction. However, continual hydrothermal activity reduces the strength of fresh rock, especially due to clay alteration and increased pore pressures (Day 1996; Voight and Elsworth 1997). This leads to a mechanically unstable edifice that deforms until either catastrophic collapse occurs, or a stable shape is regained. Catastrophic failure potential is directly associated with this kind of situation, and numerous examples in nature underline the frequent link between altered materials and flank failures (Wallace and Waythomas 1999; Komorowski et al. 1999; Siebert 1984; Siebert et al. 1987; Swanson et al. 1995) making this deformation particularly interesting in hazard evaluation.

At Casita, the characteristic structures are normal faults cutting the upper flanks, thrusts at the base and strike-skip faults that relay deformation between thrusts and normal faults. The shape produced is concave-convex-concave, due to mid-flank steepening and summit region flattening. A large horseshoe-shape scarp on the southeast flank of the volcano corresponds to a gravita-

Editorial Responsibility: J. Gilbert

E. Cecchi (✉) · B. van Wyk de Vries
Laboratoire Magmas et Volcans, UMR6524 du CNRS, OPGC,
Université Blaise Pascal,
Clermont Ferrand, France
e-mail: Cecchi@opgc.univ-bpclermont.fr

J.-M. Lavest
LASMEA, UMR 6602 du CNRS,
Université Blaise Pascal,
Clermont Ferrand, France

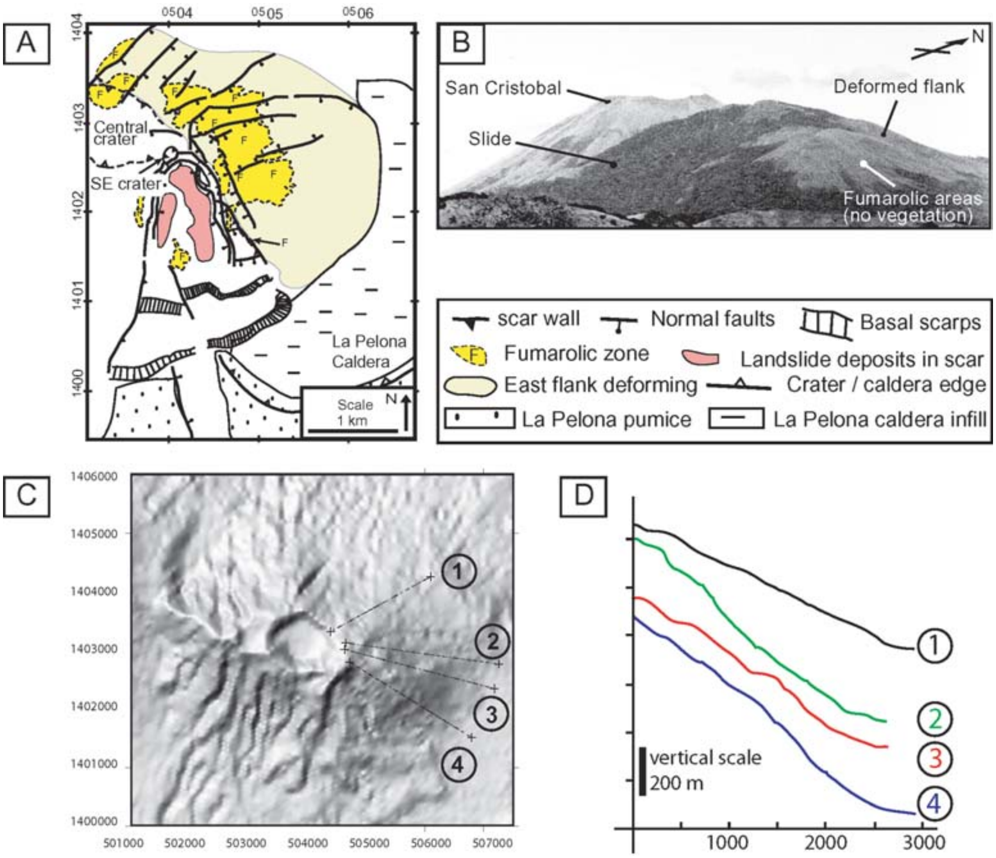

Fig. 1A–D Casita volcano, Nicaragua. Adapted from van Wyk de Vries et al. (2000). **A** Structural map of the deformed flanks of Casita showing the south gravitational slide with its well-formed horse-shoe scarp, and the east flank deformation. **B** Picture of Casita showing its deformed topography and altered areas. Another volcano in the background, San Cristobal, shows the morphology difference between a deformed and undeformed volcano. **C** DEM of Casita where flank sections of (**D**) are located. **D** East flank sections showing deformation: concave-convex-concave or convex-concave profiles

tional slide deeply-rooted in highly altered rock, and a weak pumice layer (Fig. 1). While the connection between deformation and hydrothermal alteration appears clear at Casita, the relationship between the position and extent of alteration and the style of deformation is unclear. It is necessary to characterise such deformation if it is to be detected and analysed at other volcanoes. For this reason we have carried out an analogue study to determine the structures produced by various geometrical configurations of altered and fresh rock.

Hydrothermal activity and edifice weakening

Active volcanoes generally have a well-developed hydrothermal system. Each hydrothermal system has its own distinctive size, volume, chemical and physical characteristics and develops in a unique way. A hot, pressurised fluid circulation is generated and maintained by intrusive bodies. A mixture of infiltrating meteoric water and magmatic fluids interacts with host rocks, producing brines rich in corrosive chemicals. The fluids thus acquire an important alteration potential (Lopez and Williams 1993).

Rock alteration and high fluid pressure are two phenomena developed by hydrothermal activity that can weaken an edifice. Hydrothermal alteration is a general term grouping mineralogical, textural and chemical rock changes in response to changes of the thermal and chemical environment including fluids (Wohletz and Heiken 1992). Alteration processes consist of rock dissolution and precipitation of altered minerals in the free porous space and in fractures. Depending on pressure, temperature and chemical composition of water, dissolution or precipitation will be active in preferential zones inside the edifice. Dissolution is more efficient when pressure and temperature increase (Day 1996).

Hydrothermal alteration greatly modifies the physical properties and behaviour of rocks that lead to a weakening of the volcanic edifice. Changes of rock properties depend broadly on the alteration process type (dissolution or precipitation) and the nature of altered minerals precipitated.

The fact that alteration processes can change in space and time means that physical properties of rocks also change spatially and temporally. When precipitation dominates, cohesion and density may increase. Free space is reduced and heavy minerals precipitate. The substitution of a mineral by one of lower density can also occur, such as clay replacing olivine or pyroxene, and can locally reduce density. Porosity and permeability decrease as secondary minerals precipitate and clay forms in the free space. The appearance of clay can significantly decrease the friction coefficient (Day 1996). Rock viscosity can decrease when the temperature and pressure conditions of a hydrothermal system rise. When dissolution dominates, the opposite effects from precipitation are expected for most parameters: decrease of cohesion and density and an increase in porosity and permeability. It is more difficult to assess the modification of viscosity and the friction coefficient in this case. It is thus difficult to predict the general behaviour of altered rock masses, although a strength decrease is a good approximation for clay-rich altered rocks.

High pore pressure is very efficient in weakening rocks, probably much more so than the physical modifications of rocks during alteration (Day 1996). High fluid pressure in the hydrothermal system favours fracturing and results in a loss of strength. Furthermore, altered rocks are more likely to permit very high pore pressure compared with fresh rocks as cumulative fluid pressure increases can occur in zones surrounded by areas of low permeability. Altered rocks can be brittle at small scales or at high strain rates. Modifications of rock composition, such as creating a large clay fraction or secondary minerals like quartz can, however, favour ductile behaviour (Petley and Allison 1997; Fournier 1999). Fluid presence will have a similar effect. When pressure and temperature conditions are relatively high, and when strain rates are quite low (10^{-12} s^{-1} for example), altered rocks can adopt a ductile behaviour at edifice scale, even if the mechanism is brittle at a smaller scale. This phenomenon has been revealed in laboratory experiments on clay samples (Petley 1996).

In summary, intense large-scale fracturing of rocks associated with hydrothermal fluids and the combination of physical, chemical and mineralogical modifications generated by hydrothermal alteration lead to edifice weakening. Compared with fresh volcanic rocks, altered rocks form regions of low strength, and ductile response can be expected under gravity, resulting in edifice deformation and destabilization.

The 3D extent of the hydrothermal system can be approximated by observing surface manifestations (fumaroles, hot springs, apparent altered areas), geophysical studies and drilling. Surface features give only a very rough idea of the scale of the hydrothermal system, and the other methods are very costly. Besides, as the hydrothermal system can vary rapidly with edifice evolution, it can become quite difficult to locate regions affected by the hydrothermal activity.

Analogue modelling

Model scaling

The analogue models are a development of those presented in van Wyk de Vries et al. (2000). They use two types of material, a granular mix of sand and plaster to simulate fresh volcanic sequences, and a silicone putty to simulate altered areas (Fig. 2). Such materials are commonly used in analogue models and the scaling and physical properties are well known (e.g. Merle and Borgia 1996; van Wyk de Vries et al. 2000). A Mohr-Coulomb rheology characterizes the cohesive granular material and the silicone has a Newtonian behaviour when pure and a Bingham behaviour when mixed with sand. Physical properties of the materials used are listed in Table 1.

First approach

For a first approximation our models are scaled using established analogue procedures (Merle and Vendeville 1995; Hubbert 1937; Ramberg 1981) to make sure all forces, lengths and times are realistic (Table 1). The length scale is taken to be 10^{-4} where 100 m in nature is 1 cm in the model. Density scales at about 0.5 (rock is about 2650 kg m^{-3}, sand-grain mixtures about 1400 kg m^{-3}), and gravity acceleration is the same for model and nature. A good approximation of stress is the product of length scale, density scale and gravity scale and thus is about 10^{-5}. Cohesion also has units of stress and scales accordingly, thus the cohesion of the granular material should be 10^{-5} times less than the prototype. Cohesion in volcanic edifice rocks varies enormously, from near cohesionless scoria layers, to massive lavas with cohesions of up to 10^{7} Pa. Pure sand is effectively cohesionless (Claudin 1999), but mixing plaster and sand creates a cohesive material up to 100 Pa, and so scales appropriately in the models.

Viscosity is a major unknown in volcanic edifice rocks. Intact, fresh volcanic rocks probably have viscosities of 10^{21} – 10^{22} Pa.s (Ramberg 1981) and are effectively brittle on volcanic edifice timescales. Altered regions where clay contents are high should have viscosities similar to those of clay-rich sediments (very clay-rich to clay sediments present viscosities of 10^{17} – 10^{19} Pa.s). High pore pressures may lower this value by several orders of magnitude (Cobbold and Castro 1999). Some types of alteration may raise viscosities, while magma, if present, will lower it. Magmatic intrusions such as cryptodomes may have bulk viscosities of 10^{11} Pa.s or less (Alidibirov et al. 1997).

Our silicone has a viscosity of 4×10^{4} Pa.s when pure and 10^{5} Pa.s when mixed with 20% sand (Girard 2002). Scaling viscosity thus gives a ratio of 4×10^{-13} if we decide to take the clay-rich case, as edifices are often highly altered and other factors (such as elevated pore pressure) also lower the viscosity.

Time in the models is calculated from the viscosity scale (μ^*) and the stress scale (σ^*):

$$\sigma^* = \mu^* \cdot \dot{\varepsilon}^*$$

with

$$\dot{\varepsilon}^*$$

the deformation rate ratio:

$$\dot{\varepsilon}^* = \frac{1}{t^*}$$

Using the silicone viscosity value, the time scale (t*) is found to be 4×10^{-8}, so one second in the model relates to about 0.79 years in nature. The models can be scaled to relate to other viscosities (such as lava and less-altered

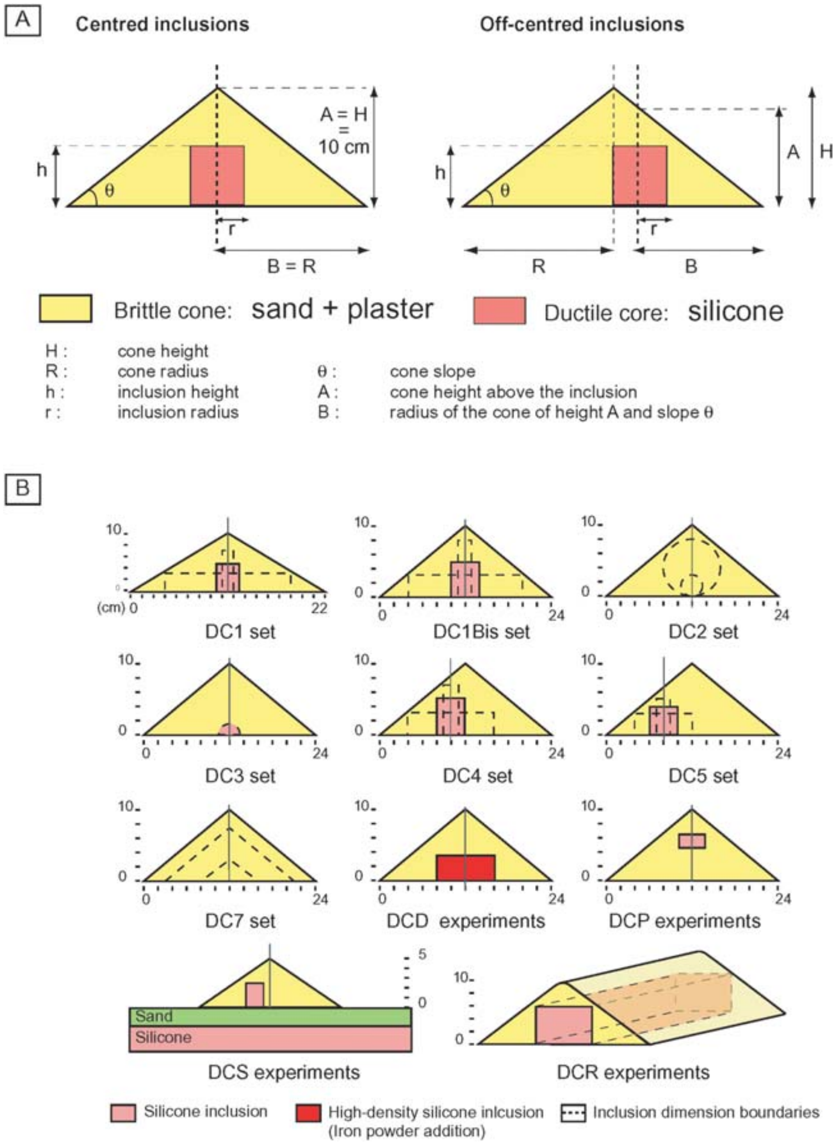

Fig. 2A,B Analogue models. **A** Sketches of an inclusion centred model and an off-centred inclusion model, with the different important geometrical parameters. **B** The different sets of experiments done

Table 1 Scaling: Geometrical and mechanical parameters of scaling and their values in (1) nature, (2) models, (3) nature calculated from scaling

Variables		Values			Units
		Nature (literature)	Models	Nature (calculated from scaling)	
H	Volcano height	0.1×10^3–5×10^3	0.1	1×10^2–5×10^3	m
R	Volcano radius	2×10^2–2×10^4	1.2x 10^{-1}–1.7×10^{-1}	1.2×10^2–8.62×10^3	m
h	Ductile core height	?	1.5×10^{-2}–8×10^{-2}	1.5×10^1–4×10^3	m
r	Ductile core radius	?	1×10^{-2}–9×10^{-2}	1.5×10^1–5.22×10^3	m
ρ_v	Volcanic cone density	2.5–2.8×10^3	1.4×10^3	2.5–2.8×10^3	kg m^{-3}
ρ_s	Ductile core density	2–2.5×10^3	1×10^3	1.8×10^3–2.5×10^3	kg m^{-3}
t	Deformation time	?	10^2–4.32×10^5 (5 days)	1.07×10^9 (34 years) – 3.08×10^{14} (9.8 Ma)	s
μ	Ductile core viscosity	10^{17}–10^{19}	4×10^4	10^{17}–10^{18}	Pa s
Φ	Internal friction angle	30°	30°	30°	
τ_0	Cohesion	10^6	50	10^6	Pa
g	Gravity	9.81	9.81	9.81	m s^{-2}

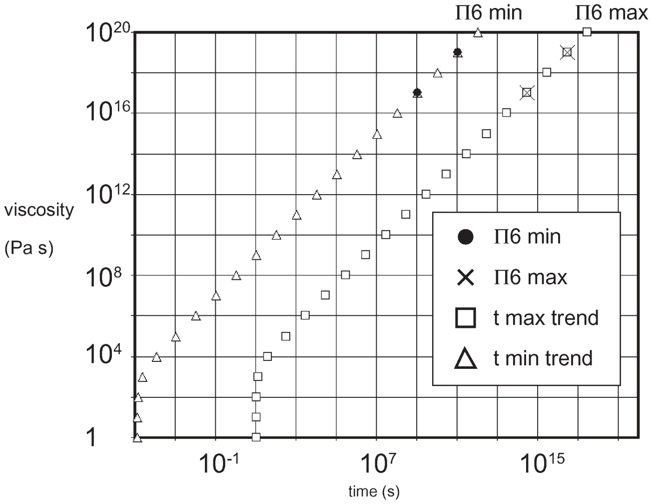

Fig. 3 Scaling of time and viscosity. Diagram showing values of Π6 calculated according to the scaling done (points). It also shows the range of time and viscosity for which the analogue experiments remain scaled (trends)

rock); the time scales related to such scenarios are given in Fig. 3.

Buckingham Pi-Theorem approach

We have also considered a dimensionless number approach similar to that of Merle and Borgia (1996). Such an approach scales the models and can help to evaluate the relative importance of the various parameters. The approach consists of establishing dimensionless numbers with all the important parameters of the studied phenomenon taken into account. These numbers have to be similar in nature and in the laboratory, given the natural values for which the models are scaled. Merle and Borgia (1996), studied a cone on a brittle-ductile two-layer base. Here, the ductile element is included within the cone (Fig. 2), and geometric parameters are different; however, the forces involved are similar.

There are 11 variables in our system and 3 dimensions, thus 8 dimensionless numbers are required to characterise the system (Table 2). The first three numbers are geometrical characteristics. The others represent the forces, either implicitly such as in Π_4 (where unit mass is considered), or explicitly with the forces of gravity, viscosity, inertia, and failure resistance (described as unit surface forces). Formulae of these Π numbers are expressed in Table 3.

The dimensionless numbers allow us to define the characteristics of the system:

Π_1 is the average volcano slope and an indication of the volcano type: stratocones have high values and shields low values. We expect in general that higher values indicate greater potential for deformation, due to steeper slopes.

Π_2 is the ratio between the height of the volcano and the height of the soft core. It provides a measure of the force exerted on the ductile core; accordingly, the higher this value, the greater the rate of deformation expected.

Π_3 gives the distance of the ductile core from the free surface, and thus the restraint provided by brittle rocks on viscous deformation. The smaller this value the lower the resistance.

Π_4 is the difference in unit mass (or density) of fresh and altered rock. The effect of this number is more difficult to evaluate; higher density of the volcanic materials may cause higher deformation rates. In the models, we found that changing the silicone inclusion density had no detectable effect on the deformation rate, while increasing the density of the sand mix did increase deformation rate.

Π_5 and Π_6 are balances of the driving and resistive forces of the system. The gravity acceleration being constant, Π_5 is controlled by viscosity, and is thus proportional to the deformation. Π_6 is a modification of the Π_6 of Merle and Borgia (1996), to include the effects of cohesion. In fresh volcanic rock the failure resistance is dominated by cohesion, and in volcanoes this can vary from 0 to 10^7 (loose scoria to strong fractured rock). We take the higher value for our highest cohesion in our sand mix. Likewise, viscosity can vary by several orders of magnitude for altered rock, and by 10 orders if the inclusion is magmatic. Π_6 could potentially be highly variable and spans the range of volcanic landforms. For example, an active lava dome has a low resistance (rubble carapace) and a low viscosity core, so Π_6 is high. At the other extreme a lava shield with little alteration would have low Π_6. For further refinement, the effective stress could be considered to take into account pore pressure effects. Note that an increase in fluid pressure would reduce the viscosity, and thus Π_6 would be higher, meaning a higher tendency of rocks to fracture.

The viscosity of rock presents a particular problem for scaling. Little is known about the apparent viscosity of

Table 2 Scaling: Π numbers and their values

Π Number	Description	Model values
Π_1	Volcano height / volcano radius	0.58–0.83
Π_2	Volcano height / inclusion height	1.25–6.66
Π_3	Volcano radius at inclusion height / inclusion radius	0.33–9.77
Π_4	Volcano density / inclusion density	1.40
Π_5	Gravity force / viscous force	$0.68–1.26\times10^5$
Π_6	Mohr Coulomb failure resistance / viscous force	$1.05–5.75\times10^3$
Π_7	Inertial force / viscous force	$1.28\times10^{-10}–1.57\times10^{-5}$
Π_8	Internal friction angle	30°

Table 3 Scaling: Π number and force formulas. Forces are expressed by surface unit. See Table 1 and Fig. 2 for the variable and Π number definition. The difference in core height at volcano height (H-h) is H' and is analogous to the volcano height (H) of Merle and Borgia (1996). Both represent the topographic potential applied on the ductile body. H' is thus used for the gravity force and the Π_6

Π numbers and forces	Formulae
Π_1	H/R
Π_2	H/h
Π_3	R'/r
Π_4	$\frac{\rho_v}{\rho_s}$
Π_5	$\frac{\rho_v\, g(H-h)t}{\mu} = \frac{\rho_v\, g\, H'\, t}{\mu}$
Π_6	$\frac{t\left[\tau_0\left(1+2\tan\Phi\left(\frac{1+\sin\Phi}{1-\sin\Phi}\right)^{-\frac{1}{2}}\right)+\tan\Phi\,\rho_v\, g\, H'\left(1-\left(\frac{1+\sin\Phi}{1-\sin\Phi}\right)^{-1}\right)\right]}{\mu} + \tan\Phi$
Π_7	$\frac{\rho_s\, g\, h^2}{\mu\, t}$
Π_8	Φ
Gravity force	$\rho_v\, g\, H'$
Inertial force	$\frac{\rho_s\left(\frac{h}{t}\right)^2 h}{h} = \frac{\rho_s\, h^2}{t^2}$
Viscous force	$\frac{\mu\left(\frac{h}{t}\right)}{h} = \frac{\mu}{t}$
Failure resistance force	$\tau = \tau_0 + \sigma\tan\Phi = \tau_0 + (\sigma_1 - \sigma_3)\cdot\tan\Phi$ from Navier-Coulomb criteria with $\sigma_1 = \rho_v\, g\, H'$ with $\sigma_3 = \frac{\sigma_1 - a}{b} - \frac{\mu}{t} = \frac{\rho_v\, g\, H' - a}{b} - \frac{\mu}{t}$ (cone load + viscous deformation) with $a = 2\sigma_0\sqrt{b}$ and $b = \frac{1+\sin\Phi}{1-\sin\Phi}$

altered rocks. A range of viscosities has to be considered first, depending on the nature of alteration. If the altered body is clay-rich, its viscosity can be compared to clay rich sediments that have values of 10^{17} – 10^{19} Pa.s. If we consider that regions affected by the hydrothermal system present a high fluid pressure that tends to reduce the viscosity, we can assume that these are maximum values.

To check if our viscosity values are appropriate we take the case of Casita volcano, where the age of flank spreading is roughly known. The age allows us to use the Π_6 number to calculate the viscosity of the weak core at Casita. To do this we also need to define the approximate geometry of the core: the depth below the summit of the core top (H') is estimated at 280 m (H' calculated with H = 1400 m and Π_2 = 1.25). In addition, the Π_6 value is fixed at the lower estimated value (1.05), as Casita's edifice is highly fractured, and consequently has low cohesion. Other values such as density are those in Table 1 (column 3).

The time (t) for deformation to appear is estimated from the fumarolic activity that has existed for 5 centuries (Hazlet 1987) and the last summit-building eruption that has been dated at 8330 ± 50 BP (Vallance et al. 2003). Consequently, deformation began at least 500 years ago and is less than 8330 years old. From the Π_6 number, the viscosity is calculated for the two limit dates. If t = 500 years, $\mu_N = 1.49\times10^{17}$ Pa.s, and if t = 8330 years, $\mu_N = 2.48\times10^{18}$ Pa.s, which are values that are coherent with our scaling assumptions.

Π_7 is the balance of inertial and viscous forces. Inertial forces in nature and the model are extremely small as velocities are low. However, Π_7 increases when the volcano deformation changes to a fast moving landslide. This can happen in nature where fractured rock changes its state to a flowing granular material; however, this is not possible with silicone.

Π_8 is the angle of internal friction. It is not highly variable as internal friction angles remain between 30° and 40° in fresh rocks.

For the models, these Π numbers have to be similar to natural values. Table 2 lists the Π numbers calculated using model values and natural values taken from the literature (columns A and B of Table 1). This approach allows to calculate the natural values for which the experiments are scaled.

Experimental procedure

The initial model is based on a simple sand cone set on a rigid support with a silicone core. Because the hydrothermal system develops around magmatic bodies inside and beneath the volcano, the inclusion was placed at the base of the cone. Nine sets of experiments were run with different inclusion sizes, shapes and positions (Fig. 2). Inclusion shapes were cylinders, spheres, hemispheres, cones, and amorphous irregular volumes. Inclusions were either axisymmetric or placed off-centre. A set of exper-

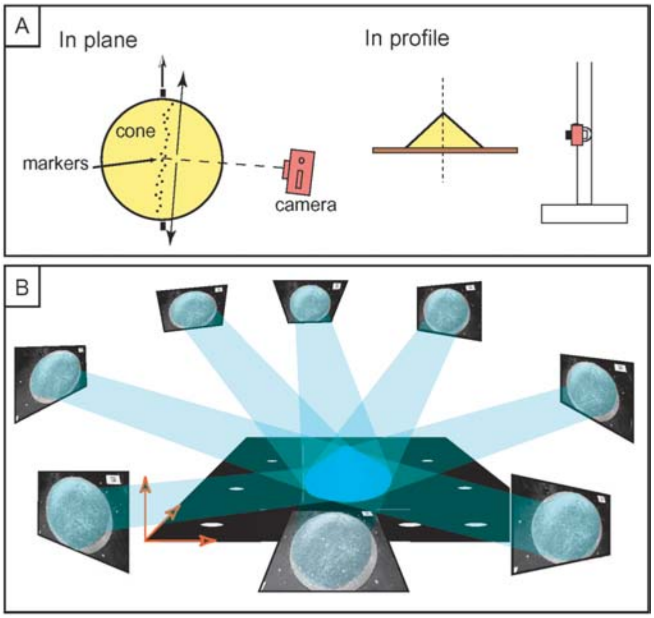

Fig. 4 A Acquisition procedure for displacement profiles. Device showed in plan and in profile. Markers are placed over the cone and a picture sequence is taken parallel to the deformation axis. Image analysis gives point displacements in the (XZ) plane. **B** Acquisition procedure for DEM generation. Multiple oblique views are taken rapidly around the model. It gives an image sequence that is used for 3D reconstruction. Different image sequences in time allow quantifying the Z deformation and following morphological changes

iments was also undertaken with a sand ridge and elongated inclusions.

In a second set of experiments we introduced a curved slope, more realistic for convex stratovolcano profiles and concave shield profiles. Lastly, we combined the Merle and Borgia (1996) spreading experiments with ours to test the influence of volcanic spreading on a ductile substratum and flank spreading due to a weak core. The start of an experiment is defined as the finish of the construction stage, and the end is defined as the time when structures have become well-developed. In the case of rapid deformation silicone quickly pierced the surface and began to flow down the cone. This was defined as the end of the realistic model, as geologically unreasonable structures developed (silicone flows). Other experiments did not deform; consequently, the experiment was terminated after a time that corresponded to the maximum reasonable lifespan of a volcano (about 1 Ma).

Models can be constructed quickly, and many repetitions and variations are possible. Initially, the deformation of the models is observed visually. Then, the models are photographed, and the deformation is recorded by images, fault maps and cross-sections. To obtain sections, the models are wetted after the run to increase cohesion and cause the plaster to set. Subsequently, they are cut rapidly into sections to avoid silicone flowage. These steps form the basis of a qualitative analysis of the experiments.

Deformation is also measured by several additional methods in order to carry out a quantitative analysis. The simplest approach is based on the analysis of sequential images taken either in profile or vertically. Deformation profiles have been obtained with the first picture acquisition method (Fig. 4 and Fig. 6). No rigorous correction of the image is done because the deformation is tracked on a plane parallel to the image plane which reduces image measurement errors. Optical distortion of the sensor is also neglected as work is done on an image sequence.

Full 3-D reconstruction of the model is possible by stereo pair analysis (Donnadieu et al. 2003) or multiple image digital photogrammetry (Cecchi et al. 2003). The latter method was used to generate accurate Digital Elevation Models (Fig. 4 and Fig. 8).

Model results

From the range of models tested we have found three principle styles of deformation. There are models where deformation is non-existent or so slow as to be geologically unimportant (taking the equivalent of several million years to form) and where subsidence is limited to the formation of a pit. These occur with volumes of silicone below a certain threshold. Above this limit, deformation either involves the whole cone (symmetrical) or only one flank (asymmetrical), depending on the original position of the ductile core.

Geometry of deformation

Pit-type deformation

For the pit-type experiments deformation was limited to a small annular fault directly above the silicone inclusion (Fig. 5). The collapse had the form of a piston-like subsidence similar to a pit-crater. Probably the summit load was high enough to cause failure of the sand at the roof of the inclusion. Deformation stopped when this load became equal to the resistance of the sand. The central block had subsided several millimetres for small (<3 cm) diameter inclusions. For wider inclusions, silicone rise intersected the surface if left for a long enough time. In this case the summit continued to collapse. Such an experiment is not representative of higher-viscosity hydrothermal altered cases, but could represent low-viscosity magma intrusions and pit crater formation.

Symmetric deformation

Symmetrically placed large volume inclusions caused deformation all around the cone (Fig. 5). The summit sagged down into the inclusion, and small concentric near-summit thrusts developed. Radial and concentric fractures and faults developed in a ring outside the summit sag. The flanks outside the ring of structures became steeper and thrusts and landslides developed on the lower flanks. In

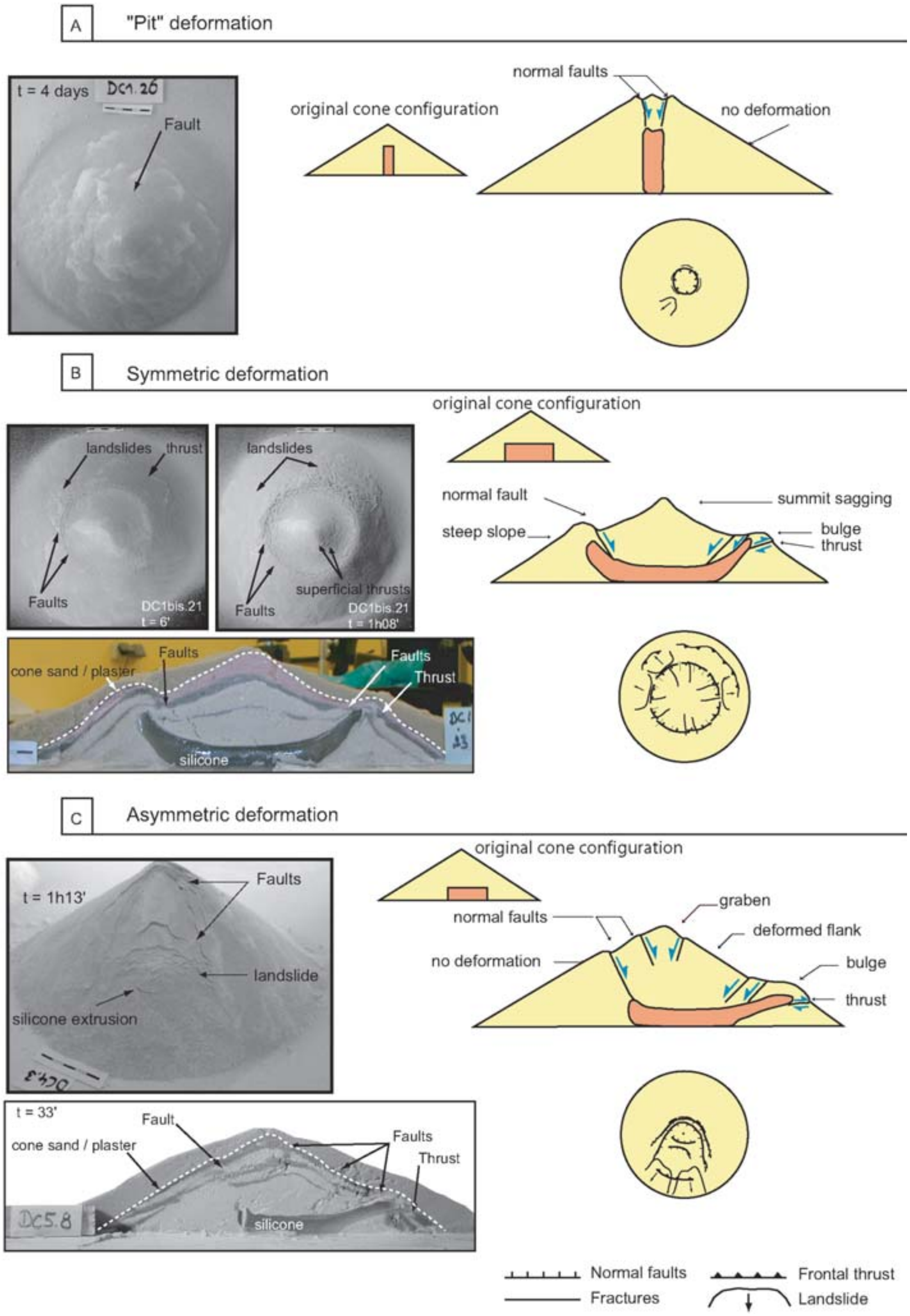

Fig. 5A–C Experimental results: the three deformation types. **A** The pit type deformation: one picture and two diagrams (profile and plane) describe the deformation observed, that is normal faults developing above the inclusion and creating a pit. **B** The symmetric deformation type. Two pictures show one symmetric experiment at different times. The third picture corresponds to a cut section. Deformation, drawn on two diagrams, consists of summit sagging and mid-flank bulging, with normal concentric faults and radial fractures developing at the transition. Thrusts develop early at the bulge foot and landslides occur where slopes get steeper. A gentle asymmetry is generally observed. **C** The asymmetric deformation type. Preferential spreading occurs with normal faults developing at the cone summit, sometimes grabens, and thrusts at the front slump. A bulge appears and leads to frequent landslides

most models a slight asymmetry developed with one flank spreading out more than the others, as models are never perfectly symmetric.

The initial linear slope is modified to produce a concave-convex-concave profile. The summit sagging produces the upper concavity, and the bulging fractured region the convexity, while the lower steepened area is concave down to a lower undeformed region.

In the sagging area, the deformation style depends on the thickness/width ratio of the inclusion. When this ratio is high (i.e. the inclusion is a tall cylinder), the summit sags strongly and concentric thrusts are developed. However, when the ratio is low (i.e. the inclusion is tabular) the summit sags less, but spreads laterally with the development of radial grabens. This effect is similar to that described for volcanoes spreading on weak substrata by van Wyk de Vries and Matela (1998).

In all cases the inclusion has a characteristic bowl shape after deformation. Initially, the sides of the inclusion start to spear outwards and up as the central part is depressed. The side of the inclusion displaces the sand and bends up the adjacent layers. The sand develops a thrust along which the silicone pushes up.

Asymmetric deformation

Asymmetric deformation is found when the silicone inclusion is off-centre (Fig. 5). In these models the deformation is mostly in the direction of the asymmetry. A series of arcuate normal faults develops around the summit, which relay via en-echelon strike-slip faults to a flank thrust. An antithetic normal fault develops around the summit, making a small summit graben when deformation is well advanced. Other normal faults develop on a bulging region above the thrust. The thrust is rapidly cut by landslides from the bulge. Eventually, a tongue of silicone pierces the bulge. The profile along the deformed zone is again concave-convex-concave. The inclusion shape is similar to that of the symmetrical experiments, except that one side is preferentially developed into a tongue that has pushed up the fault.

Displacement profiles

Displacement profiles were generated by photographing experiments on a vertical plane (Donnadieu et al. 2003). For symmetric experiments (Fig. 6A) deformation is predominantly vertical in the upper region while for asymmetric ones (Fig. 6B) there is a marked horizontal component towards the bulge. The bulge region shows a predominantly horizontal movement, with a small downward component. Below the bulge, a small slope-parallel movement can be seen in the asymmetric profile, which corresponds to grain sliding along the steep slope.

The deformation vector also changes with time for individual points (Fig. 7). For a symmetrical experiment horizontal (X) displacement is roughly constant with time, but the vertical component (Z) is slightly larger at the beginning for the summit region. The bulge has a slight positive Z displacement initially, which then becomes negative. Asymmetrical experiments have initially rapid X and Z displacements; X becomes negligible in the summit region, at the same time as the graben develops, but outward movement continues elsewhere. Z displacements also decrease with time, and for the bulge region become positive for a period. For both sets of experiments the ratio of X to Z remains linear, except for the initial stage in the summit area of the asymmetric model.

One ‘pit’-like model was also included (Fig. 6C). Over the 13 days that it was left to deform, no flank movement could be seen; however, the profile analysis showed several millimetres of slope parallel deformation. This occurred on the first day during which the summit pit formed.

Deformation fields

Digital Elevation Models (DEMs) have been generated from image sequences taken at different times during selected experiments. The technique used is a novel 3D reconstruction approach using a multi-view analysis (Cecchi et al. 2003). In Fig. 8, DEMs for an asymmetric and a symmetric experiment are shown. Deformation structures are accurately reconstructed, even if some small errors appeared on fractures due to a lack of visual data for the reconstruction process. Errors are present at the base of the cone due to lack of texture in the image. The grain-flow patterns generated during cone construction are visible as rough lobate texture (Fig. 9). These DEMs allow quantitative description of deformation structures by analysing the Z deformation with time. In Fig. 9, Z deformation maps are presented for selected

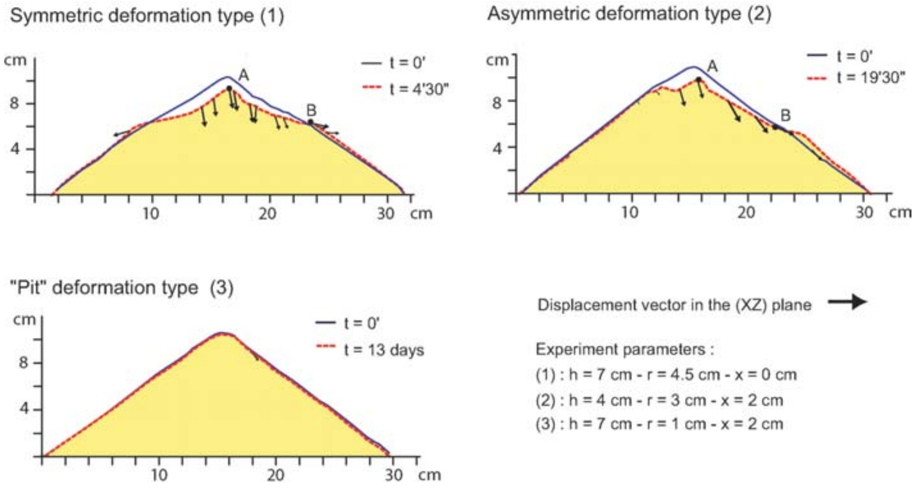

Fig. 6 Displacement profiles for each of the three deformation types. Experiment parameters are given: h = inclusion height, r = inclusion radius, x = inclusion / cone off-centring. Initial and final profiles are drawn, as well as (XZ) displacement vectors. These are proportional to the displacement amplitude. A and B are particular markers chosen for Fig. 7. The concave-convex-concave profile is highlighted for both symmetric and asymmetric deformation. Vertical displacements are dominant in the summit, whereas the central part of the cone is characterized by horizontal displacement. Note that there is a small horizontal component in the summit part for asymmetric experiments. The displacements recorded for the pit deformation type are very small and located above the inclusion (A few mm maximum)

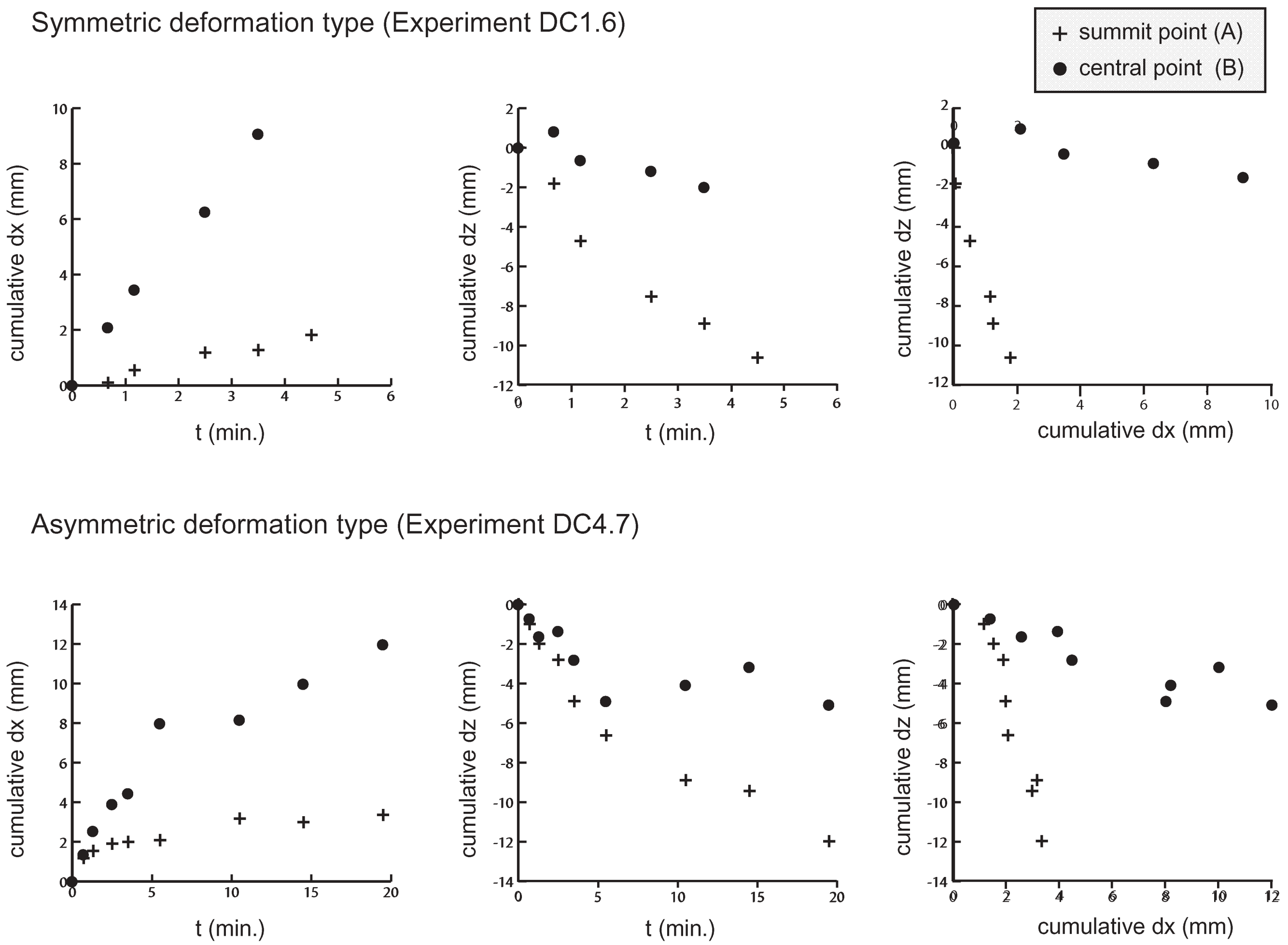

Fig. 7 X and Z displacements with time for symmetric and asymmetric experiments. Two markers are followed on each experiment, one located on the cone summit (marker *A*), and one in the upper part of the bulge (marker *B*). These specific points are located in Fig. 6. As both experiments do not have the same inclusion dimensions, direct comparison of velocities and displacement values is meaningless. The summit region is characterized in both experiments by large (more than 1 cm) and rapid negative Z displacements and by low horizontal velocity and displacements. In the central part of the cone, where the bulge forms, horizontal displacements and velocity are big compared to Z movement, and some positive Z movement appears during the point trajectory. For asymmetric deformation, horizontal and vertical velocities are bigger at the beginning of the experiment, whereas X displacement is roughly constant with time and Z slightly bigger at the beginning for symmetric deformation

experiments (symmetric and asymmetric), and a combination of deformation map, DEM and XY displacement vectors (Fig. 9C). Note that there is a slight asymmetry also in the symmetric experiment, evident from the deformation data, probably due to deviations during model construction. The Z deformation maps are obtained by subtraction of DEMs.

Symmetric deformation type

Summit sagging is visible early in the deformation process and is constant during the experiment, which is in agreement with previous displacement profiles. This sagging is relatively symmetric at the beginning, but downward movement concentrates on the left half at the end of the experiment. A large landslide, visible on the (acq3–acq4) map and on the last DEM (Fig. 8), is cutting the summit region. Slumps and slides on the central part of the cone appear early during the experiment and are characterized on the maps by depressions in high areas (blue or pale red areas in the central part) and lower zones of material accumulation (dark red areas). Positive and negative Z movements roughly equal each other, although a loss of material at the rim of the reconstructed models, due to an outward movement, could explain the excess negative Z movement seen in Fig. 9C (-15 mm against +11 mm). XY displacement vectors are plotted over the DEM and the Z deformation map between the beginning and the end of the experiment. Vectors represent about 50 points detected and followed manually in the image sequences. There is a preferential movement direction due to the slight model asymmetry. Vectors show that the horizontal movement is greatest at the transition between the cone summit sag and the flank bulge, this being related to the small asymmetry. Attempts to follow points

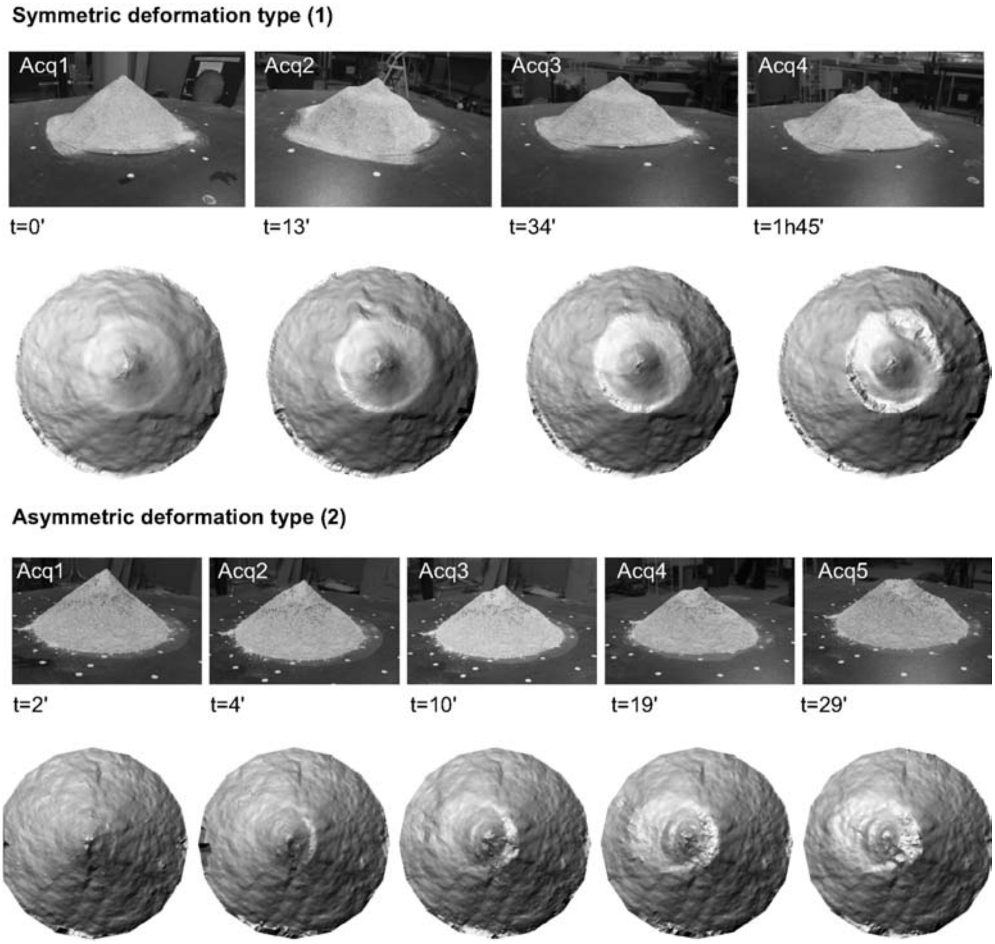

Fig. 8 3D surface reconstruction of one symmetric and one asymmetric experiment. DEMs are created from a multi-view 3D reconstruction technique. Four and five image acquisitions are done for the symmetric and the asymmetric experiments respectively. Deformation is rapid. Accurate reconstructed meshed models composed of more than 30000 triangular facets show the deformation structures and allow deformation quantification

on the bulge area failed because of the loss of texture associated to the numerous slumping events.

Asymmetric deformation type

During the early stages of deformation (first ten minutes represented by the two first deformation maps in Fig. 9B), a summit depression develops and is limited by a single horse-shoe-shaped normal fault. A bulge grows on one flank along the preferential northwest deformation axis, showing first slumps and then two slides. During the experiment, grabens develop with normal antithetic faults, while the bulge growth continues. Once again, negative and positive Z movements roughly balance each other, but there is a net negative Z movement (-20 mm against +14 mm), explained by outward movement (material outside the reconstructed area not taken into account). Reconstruction errors on the cone rims are easy to locate and can lead to over-estimation of the Z deformation, as it is the case for the acq2-acq3 map (over-estimation by +40 mm), the acq3-acq4 map (over-estimation by -26 mm) and the acq4-acq5 map (over-estimation by +24 mm) of Fig. 9B. Concerning the XY vectors shown in Fig. 9C, the horizontal movement is preferentially orientated outward along the deformation axis and increases from the summit to the depression and bulge transition.

Critical parameters in models

Analysis of the various variables can be used to determine which factors control the transition between the 3 types of deformation. Most clearly, the data show the transition between non-spreading pit-type activity and flank spreading (symmetric or asymmetric).

The dimensions of the inclusion have an effect (Fig. 10A1): both the inclusion dimensionless height (h/A) and width (r/B) must be large enough to allow spreading. This relationship alone is not sufficient to characterize inclusions of different shapes; however, the volume also gives information on the onset of spreading. The volumetric fraction, which is a relative measurement because it takes into account the cone volume, is the best parameter. A plot of the volumetric fraction against the inclusion shape (Fig. 10A2) indicates that above 10% volume all models spread. This also shows that high, thin (large h/r) inclusions do not spread.

The shape of the inclusion (sphere, cone, square, cylinder) has no appreciable effect on the appearance of

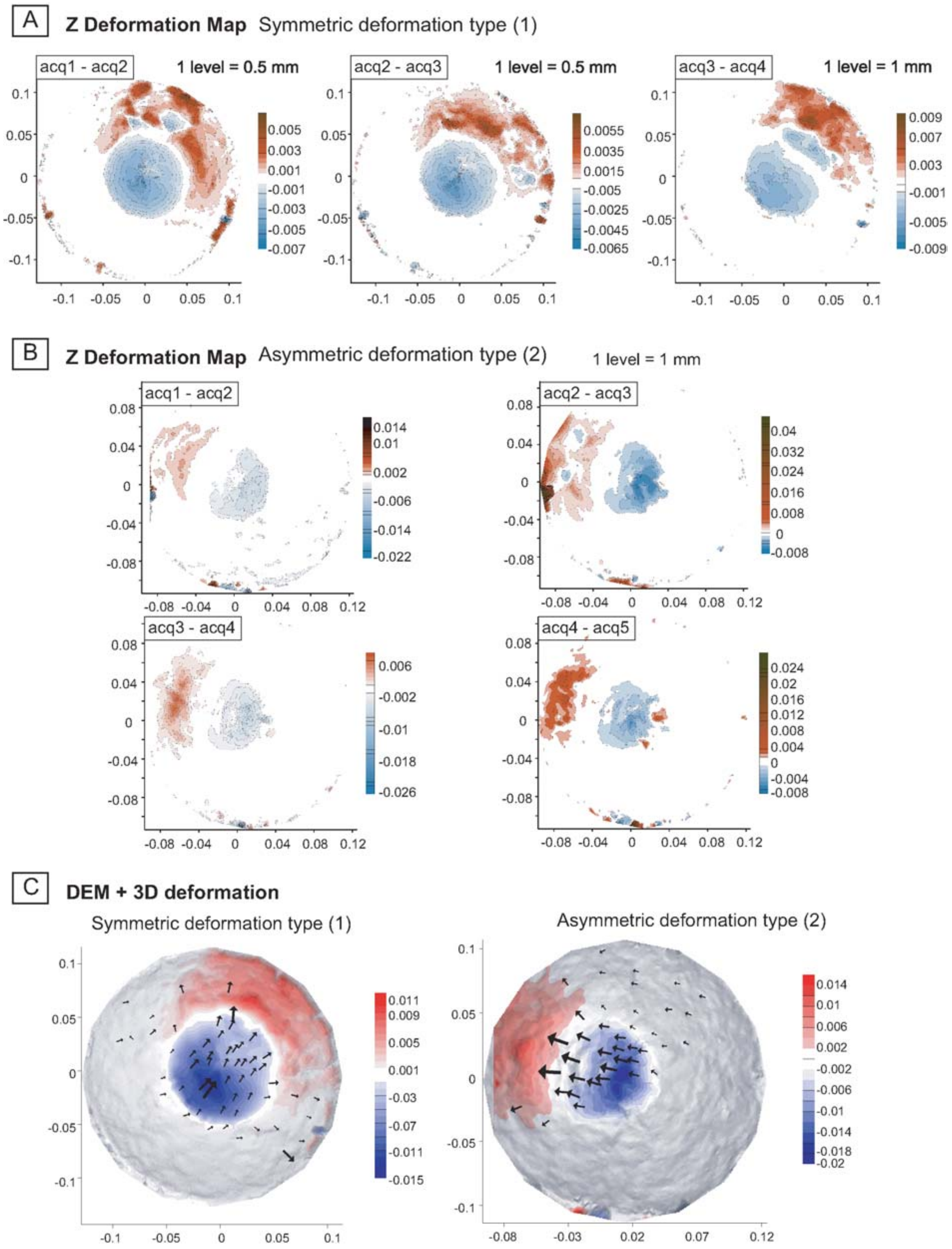

Fig. 9A–C Z deformation maps calculated from the successive DEMs (Fig. 8) for the symmetric (**A**) and asymmetric (**B**) experiments, and scattered deformation fields (XY vectors and Z map) overlying final DEMs (**C**). Z deformation maps are obtained by subtraction between two successive DEMs. Very small deformations are detected: each colour level corresponds to 1 or 0.5 mm. In (**C**), XY vectors in black represent point XY displacements between the beginning and the end of the experiments. These points are detected manually on similar view-point images at different times, with coordinates calculated on the DEM

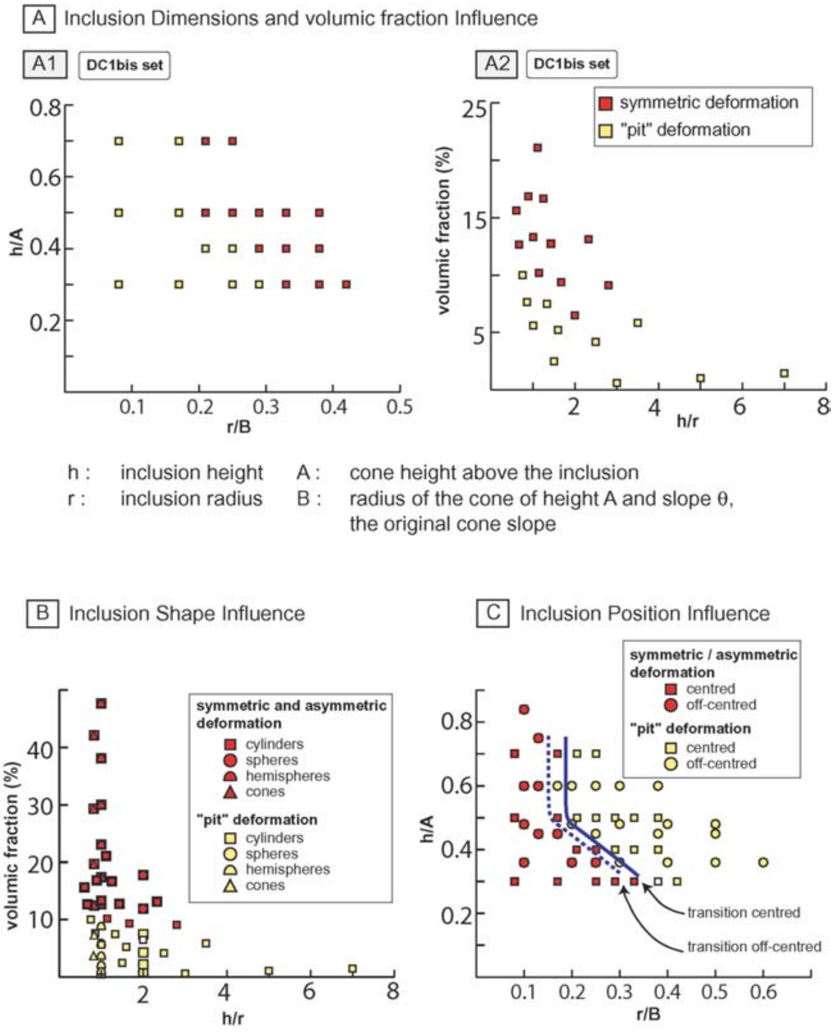

Fig. 10A–C Tested parameters and influence on the deformation type. **A** Influence of the inclusion dimensions and volumetric fraction, showed using DC1bis experiment set corresponding to centred cylindrical inclusions. **A1** For each experiment set, the deformation type is controlled by the inclusion dimensions relative to the cone dimensions, as showed with DC1bis data. **A2** Plot of the volumetric fraction against the inclusion axial ratio h/r. As different inclusion shapes are tested, volume has to be taken into account to describe correctly the transition and compare the different set results. **B** Influence of the inclusion shape on the deformation transition by plotting deformation type for the experiment sets with different inclusion shapes. No significant influence appears. The plot also shows that symmetric or asymmetric deformation can occur even for small volumetric fraction (10%). **C** Influence of the inclusion position on the transition. Deformation starts at slightly lower values when the inclusion is off-centred (closer to the cone surface)

deformation (Fig. 10B), although complex shapes create different deformation patterns.

The inclusion position has an effect on the appearance of deformation, as it brings the inclusion closer to the free surface. It also causes the change from symmetric to asymmetric movement (Fig. 10C).

Thus, it is the intimately linked parameters volume, size and position of the inclusion that mainly control the deformation. The volume required to initiate spreading is only 10% of the edifice volume.

Experiments on other volcano shapes

We made several sets of experiments on analogue volcanoes with smaller slope angles down to shields of 10°, and various shapes, such as ridges. In all these the same general deformation patterns were revealed, and the same rule applied, that at about 10% inclusion volume flank spreading occurred. It is thus important to note that under the right conditions even volcanoes of very small slope angles could evolve flank-spreading features.

Comparison with spreading and sagging models

The models presented up to this point show the effects of altered core deformation on edifices on a rigid base. However, in a lot of cases, volcanoes lie on ductile substrata and are likely to spread (Merle and Borgia 1996), or sag (van Wyk de Vries and Matela 1998). We thus conducted several experiments with cones having a ductile core and ductile substrata. In all our experiments flank spreading was the dominant mode of deformation. This is in agreement with the deformation rates measured for each type of deformation. The deformation rates in ductile core experiments are about ten times higher than in substrata spreading experiments explored by Merle and Borgia (1996). Volcanoes also can stand on sloping or dipping substrata. A few experiments were run on 0–15° sloping bases to test the effect of slope, but no relationship was found. Sloping substrata have a profound effect on substrata spreading, but this process is ten times slower than flank spreading. However, if spreading in the substrata has developed before alteration and weakening of the core, then the pre-existing structure may play a role in guiding deformation.

Natural cases

This study was inspired by the structural analysis of Casita volcano that showed that this volcano was deforming due to an altered core (van Wyk de Vries et al. 2000). Using the present model results and the geometry of Casita we can say that it is deforming in a slightly asymmetric way. Most flanks are deforming, but the southeast side is spreading preferentially, and it has initiated a large flank slump. In this slump the altered clays actually outcrop (Kerle and van Wyk de Vries 2001). The slopes of Casita show the characteristic profile, except sometimes lacking the upper concavity due to having originally a flattish summit. This symmetry and the faults define the limits of the deforming area (Fig. 1A).

We have chosen several other volcanoes for analysis, either because they show features that are most likely due to flank spreading, or because they are end-type volcanoes, such as volcanoes which are so young that it is unlikely for them to show spreading. Even if the analogue modelling simplifies the studied phenomenon, characteristic deformation patterns have been discovered on some volcanoes.

Arenal

First, we studied a young, growing stratocone: Arenal, the most active volcano in Costa Rica. If the cone was altered enough, or full of deforming magma, structures or a characteristic slope profile might be detected. Using a 25 m DEM and aerial photographs, we searched for structures on the cone. The profile is concave and does not look like a spreading one, even on the older part (East half) of the cone. There are, however, two features of interest. One is a set of steps on the East flank (Fig. 11A). We thought at first that these could be DEM artefacts (steps are common on such DEMs); however, analysis of aerial photographs allowed us to confirm their presence, and subsequently they have been field-verified (G. Alvarado, pers. comm.). Above these we also find several small fault scarps on aerial photographs (Fig. 12B). These features appear to be slight folds in the lava surface where the layers are sliding downslope on some unstable horizon (probably scoria). Such features are common on mountain slopes in layered sedimentary successions that dip downslope (Voight 1979). The higher faults may be partially compensating this sliding and may also have a regional tectonic origin (Alvarado 2003).

Despite the intense eruptive activity of the volcano, suggesting a well-developed and active hydrothermal system, no significant deformation pattern appears at Arenal. This volcano is relatively young (at least 7000 years, from Alvarado and Leandro 1999) and perhaps it has not had enough time to develop an altered rock mass big enough to deform. The particular cone construction, especially the low amounts of alteration-sensitive pyroclastics, means that it is less susceptible to hydrothermal weakening. Finally, intense eruptive activity can mask existing deformation.

Momotombo

As another example of a young stratovolcano, Momotombo, Nicaragua, was chosen. Since 1907, the date of its last eruption, this of 1258 m high symmetric cone has had strong fumarolic activity with temperatures reaching 1000°C. Aerial images show that fractures form an arcuate pattern around the summit crater (Fig. 12). The fractures diverge at the lowest part of the crater, where the 1905 lava flow exited. The sense of movement is normal at the back of the crater but is strike-slip at the sides. This pattern is similar to that observed in the asymmetric

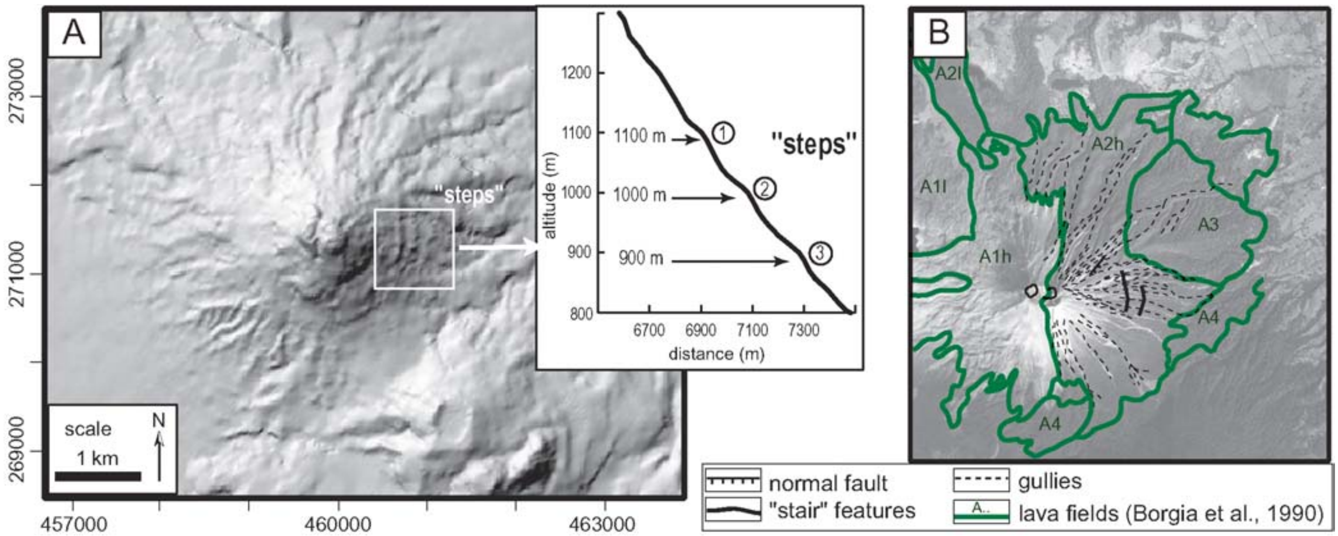

Fig. 11A,B Arenal example, Costa Rica. **A** DEM and profile detail of the East flank, showing stair-like features. **B** Aerial photograph overlaid by lava field map. Stair-like features and scarps above are located. Lava field location is from Borgia and Linneman (1990)

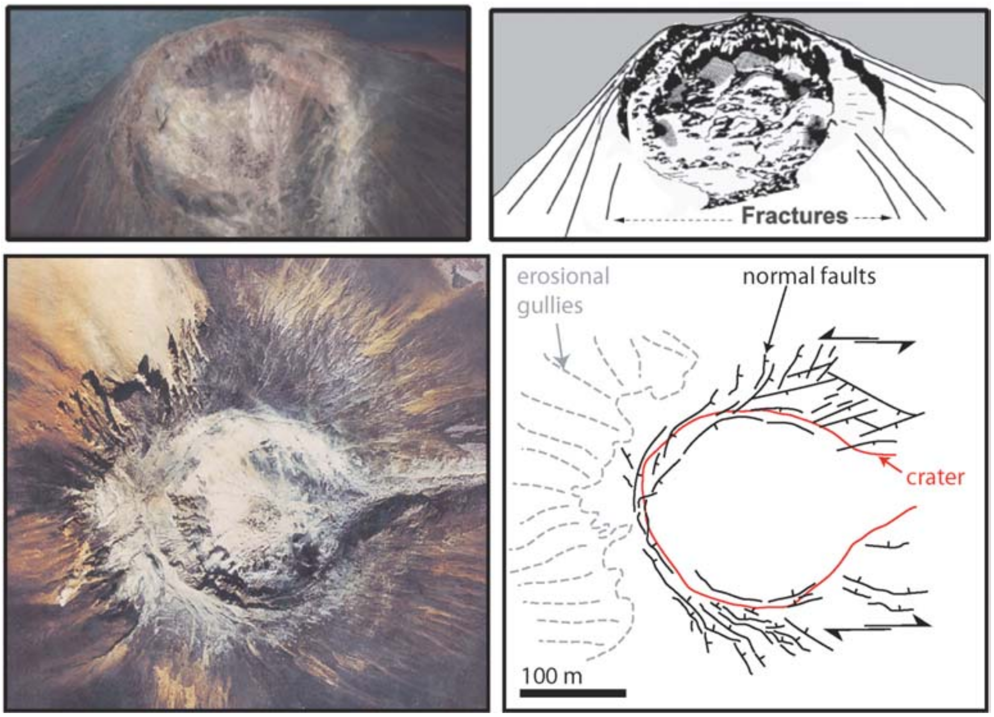

Fig. 12 Momotombo example, Nicaragua. Two photographs of the crater and sketches highlighting fractures and faults around the summit. Note that the faults outside the crater on two flanks form a strike-slip relay system like in the asymmetrical models

models. Thus, we propose that the deformation is related to progressive alteration of the summit region by the intense fumarolic activity. If the magma resident in the cone rises as a plug, it will probably displace the lower side, possibly generating a summit debris avalanche. This presents a significant hazard, although the risk of casualties is low, as the avalanche would pass into little-inhabited areas and not towards the geothermal stations on the south flank.

Telica

Telica is a shield-like volcano in northwest Nicaragua. It is cut by pronounced north-striking faults that are related to regional strike-slip motion and stress localisation by the volcanic edifice (van Wyk de Vries and Merle 1998). The volcano also hosts a major geothermal field (El Najo–San Jacinto). While investigating these features with DEM and radar images, we found that the N flank has a depressed area, and that normal faults followed a crescentic pattern around a depressed area, that is highly altered. Telica's lava-dominated shield slopes are 15° in this area, illustrating the possibility of deformation even at low angles (Fig. 13). The active crater at Telica also hosts a vigorous hydrothermal system, and to the north has a set of crescent faults; these have been previously been interpreted as buried craters. However, they may also be a small gravity slide associated with a steep step at the south base of the cone (Fig. 13).

Mombacho

We also investigated volcanoes already presenting collapse structures or important flank slides. Mombacho, a stratovolcano on the shore of lake Nicaragua, has had three catastrophic flank collapses in the past. One of them, the "El Crater" scar and deposits, is probably directly related to hydrothermal alteration of rocks and consequent edifice weakening (van Wyk de Vries and Francis 1997). Fumarolic activity is today still present and a new cone has grown on the northeast part of the edifice. This volcano again seems to be developing sliding structures on its north flank. Normal faults to the north of the summit have been identified from DEM and aerial photographs (Fig. 14A), and the northern flank shows a characteristic concave-convex-concave profile (Fig. 14B and 14C). The top 500 m section of Mombacho's north flank seems to spread and constitutes a threat in case of collapse for the city of Granada, located less than 10 km north the volcano.

Orosi-Cacao

Another example is the Orosi-Cacao andesitic complex in Costa Rica. The volcano Cacao presents two clear sliding features on its southwest and southeast flanks (Fig. 15). We digitised maps to create a DEM and used Radar images to analyse the morphology of these features. Both the southwest and southeast flank summits present steep fault scarps interpreted as slump scars, and the two sectors show basal thrusts at their feet. The southeast slump, presenting curved normal faults at the summit and flank-

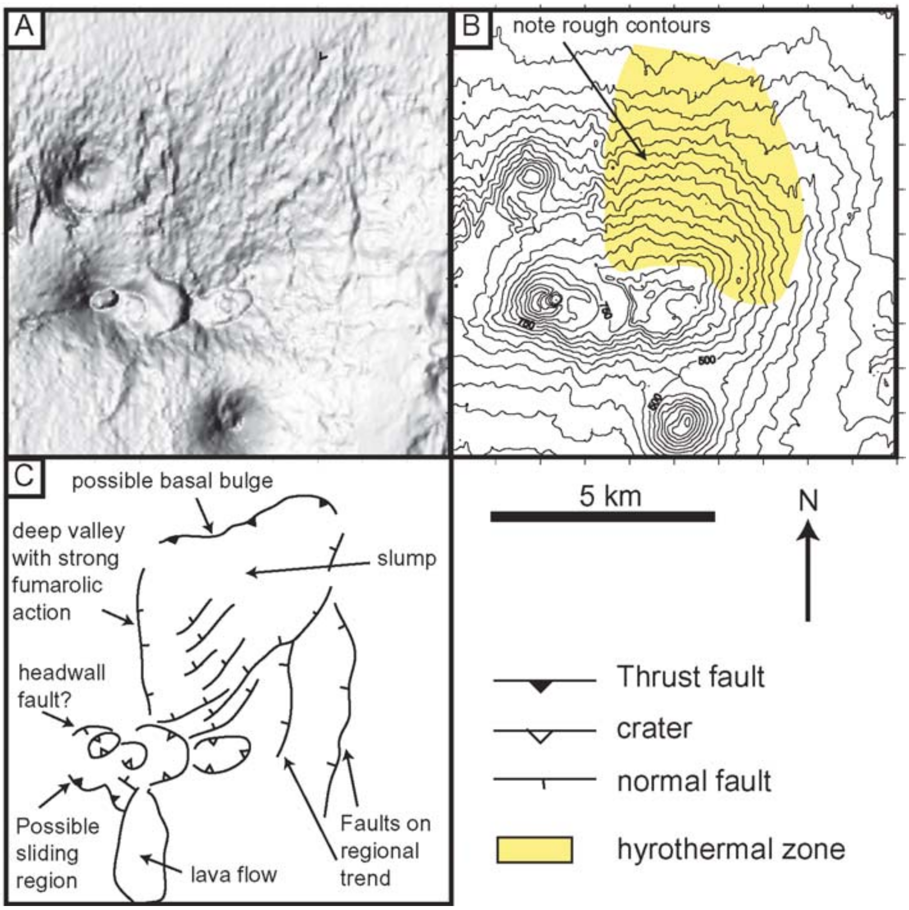

Fig. 13A–C Telica volcano. **A** Shaded relief map of Telica showing the irregular, but shallow northern slopes that are underlain by a highly active geothermal resource (El Najo). **B** Topographic map (contours every 20 m), showing the rough area on the geothermal field. **C** Interpretation of the topography in terms of normal faulting and sliding at the base. Note also the steep southern side, where the active crater area appears to be sliding as well

ing strike-slip faults, has the clearest similarity with the analogue experiments, while the southwest one is more eroded. This feature could be explained by the southwest debris avalanche deposits that have been related to partial collapse of this sector and linked to eruptive activity (Alvarado 2000). Our study confirms the slumping assumption already made by van Wyk de Vries and Francis (1997). The similarity with experimental deformation pat-terns, and the presence of rocks altered by hydrothermal activity as well as breccias and fumaroles near the volcano indicate a possible link between the observed deformation and a weak core in the edifice.

Etna

Mt. Etna is undergoing well-documented gravitational spreading due to weak substrata and intrusive complex deformation (e.g. Borgia at al. 1992; Garduño et al. 1997; Borgia et al. 2000; Froger et al. 2001). Etna is highly-active and could contain a weak core; thus, it is interesting to see if the summit morphology and structure is consistent with flank spreading. The summit area of Mt. Etna has a convex-concave-convex profile (Fig. 16). The high crater area, dominated by newly-built cones and craters, is steep sided, but flattens (concavity) on most sides. There is a possible caldera rim (Piano Caldera) exposed in several places, and below this rim the slopes become steeper. To the east, slopes drop steeply into the Valle del Bove where ground cracking and occasional small landslides have occurred (Murray et al. 1994). The morphology and structures thus appear consistent with deformation related to flank spreading: there is a horseshoe shaped head region (the Piano Caldera), a convex and concave lower-mid flank (eastern slope into the Valle del Bove), and evidence of surface instability (the cracks and landslides). Further study of these features is required as the eventual failure and collapse of such a structure would have serious hazard implications. Flank spreading would also exert an influence on the upper plumbing system of the volcano.

Other sites

The Enclos Fouqué Caldera on Piton de la Fournaise; Fogo volcano, Cap Verde, and Tenerife on the Canary islands all have structures that could be caused by flank spreading (Merle and Lénat 2003). Ruhapehu, New Zealand also has a strong hydrothermal system and has a characteristic flank spreading shape. Many volcanoes in Central and South America equally have structures and morphologies that may be caused by flank spreading. We

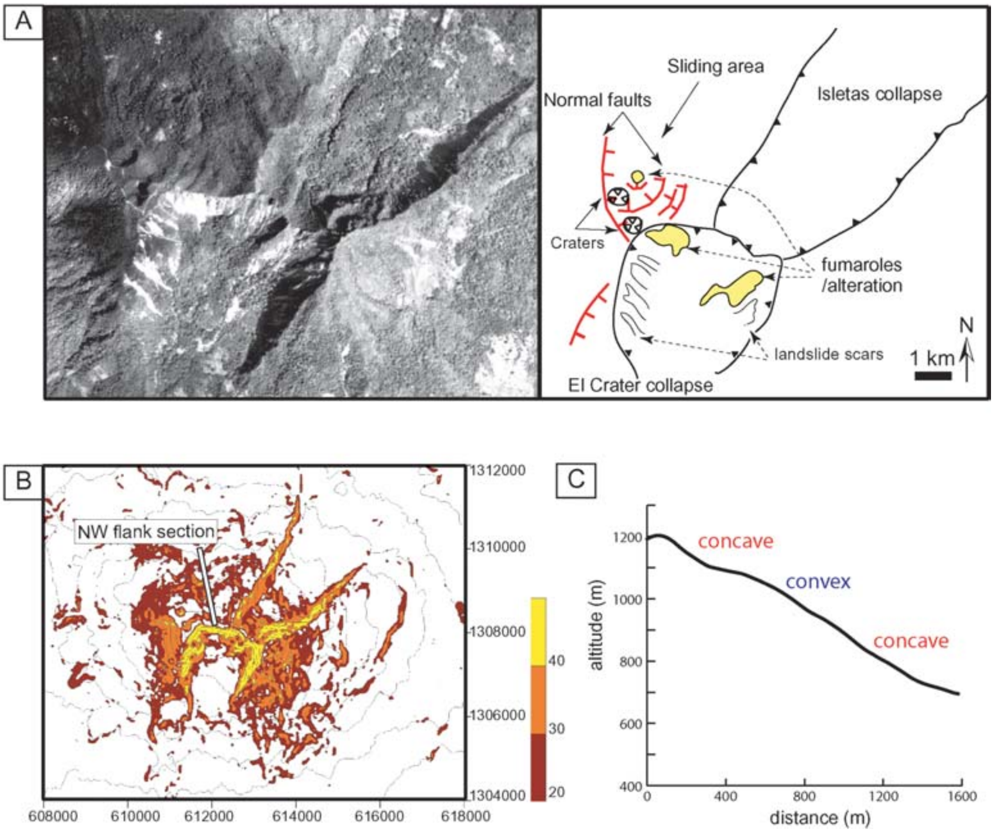

Fig. 14A–C Mombacho example, Nicaragua. **A** Aerial photo and structural diagram showing the Las Isletas and El Crater collapse scars, as well as the northwest sliding flank. **B** Slope map calculated from DEM. It shows slope steepening following topographic contours on each side of El Crater scar, particularly on the SE part, that can be related to deformation of the flanks. **C** Cross profile of the NW flank, located on B, and showing the characteristic concave-convex-concave deformation profile revealed in the experiments

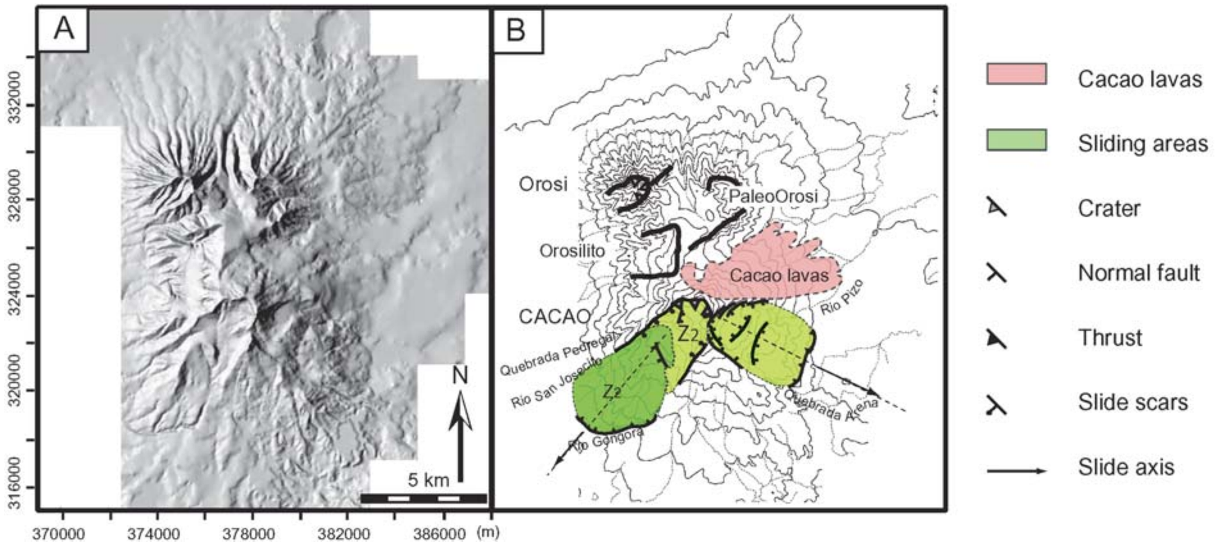

Fig. 15A,B Orosi-cacao complex example, Costa Rica. **A** DEM created from 1/50000 topographic map digitalisation. **B** Schematic structural map of Orosi-cacao showing the two sliding sectors (SW and SE flanks). *Z1* and *Z2* are two zones composing the SW sliding sector

suggest that a worldwide survey should be made using the new DEM from the Shuttle Terrain Mapping Mission to determine the number of volcanoes with this type of flank spreading.

Discussion

Our analogue modelling has showed that ductile core deformation in a stratocone or a shield volcano creates typical deformation patterns recognizable on natural volcanoes. The presence of these specific structures and displacements on natural volcanoes could indicate ductile

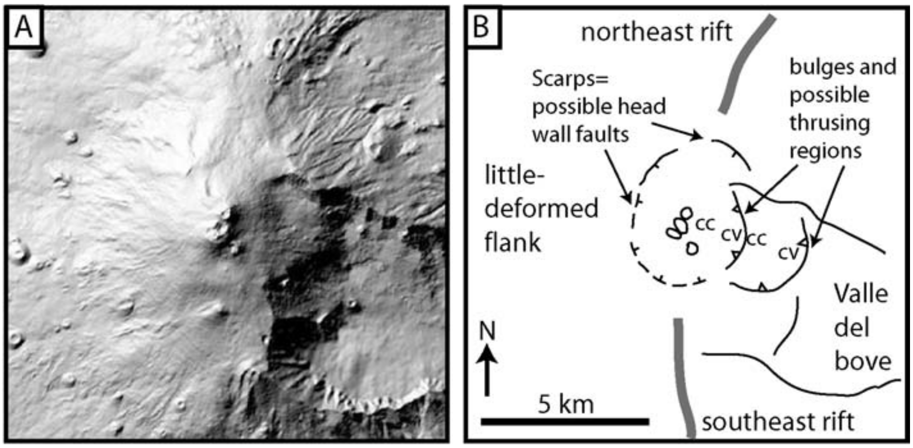

Fig. 16A,B Etna. **A** shows a shaded relief image of Etna DEM and **B** the interpretative structure and morphology. Note the double convex (*cc*) concave (*cv*) structure in the Valle del Bove slope, and the flattened summit area around the main cones. Such a morphology is consistent with flank spreading directed into the northern part of the Valle del Bove. The geometry and structure of this postulated deformation may be influenced by the substrata spreading already occurring at Etna (Borgia et al. 1992)

behaviour of an altered core. Structures also give information on the core's dimensions and location. Conversely, if the approximate spatial extent of the ductile region is known, experimental results allow us to predict the types of deformation expected (Figs. 5 and 10).

The scaling shows that for the chosen altered core viscosity two main deformation types exist in nature: symmetric and asymmetric deformation. The transition seen in experiments between the "pit" deformation type and symmetric or asymmetric deformation corresponds in fact to the appearance of deformation in nature, as deformation by 'pits' is not realistic during the average lifespan of a volcano. This "pit" deformation type could eventually occur when magma or altered areas with lower viscosities are considered. Forces controlling deformation are expressed by the Π_5 and Π_6 numbers, which are proportional to $t\ /\ \mu$. When these numbers are kept constant,, pit-type deformation becomes reasonable during the development process of a volcano if lower viscosities are chosen.

Gravitational deformation of the ductile-cored edifice is a reason for slope instability and collapses. According to the experiments, three collapse generations can be defined occurring at different stages of the deformation (Fig. 17):

Generation 1 collapses correspond to superficial failures that can occur during the gravitational deformation of the volcano. These are found in areas where slopes get steeper and where head scar faults develop. They start as landslides that can transform into small debris avalanches or into lahars. Experiments showed that they can appear early during deformation.

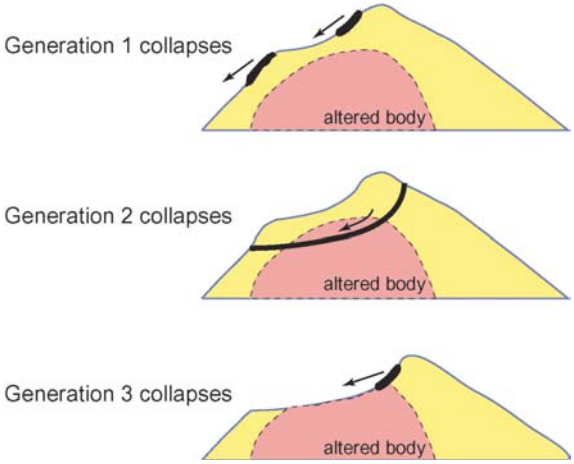

Fig. 17 The 3 possible generations of collapse during the gravitational deformation of altered core edifices. Collapse areas are located by *arrows*

Generation 2 collapses are catastrophic flank collapses that can happen after a period of progressive flank creep of variable duration. Experiments show that this type of collapse is likely to occur when deformation is asymmetric. This avalanche type does not appear in the experiments as a combination of brittle and ductile behaviour in a single analogue material was not possible. However, major faults that developed at the creep head could act as a sliding surface. In nature, such faults that develop in the brittle part of the volcano could extend into the ductile altered body. Field evidence shows that sliding surfaces can be located in altered zones (van Wyk de Vries et al. 2000). Brittle/ductile transition of altered rocks can be explained by a deformation rate increase, itself related to greater edifice instability. Various mechanisms can trigger the increase, such as magma intrusion or pore pressure increase. Micro-fracture increase and fracture coalescence in the altered body could also be an explanation for the catastrophic collapse mechanism, as proposed in studies concerning deep-seated landslides (Petley and Allison 1997). Another possibility to explain catastrophic collapse is that the altered body works like a slip layer along which the above rock mass can slide. Progressive alteration will also increase slippage.

Generation 3 collapses originate from collapse scars when unstable or altered rock bodies remain. Although they have a small volume compared with type 2, they could still be devastating. Like generation 1 collapses, they can lead to small to moderate debris avalanches and lahars.

All these collapse types can be found in nature, and field observations show that hydrothermal alteration plays a significant role in flank destabilization and the ability to collapse suddenly. Numerous examples of altered products in debris avalanches or apparent connections between altered areas and collapses have been reported. Among them we can cite the debris avalanche of Chestina in Alaska, resulting from a collapse of the Wrangell volcano, where an important fraction of the clasts was hydrothermally altered (Wallace and Waythomas 1999). Strongly altered products were also found in the 26 December 1997 debris avalanche produced by the south flank collapse of Soufriere Hills, Montserrat (Komorowski et al. 1999). At Mt St Helens, a connection between the 1980 collapse and an old altered dome has been established (Swanson et al. 1995). Siebert (1984) and Siebert et al. (1987) also outline hydrothermal system development and associated alteration in areas where collapses occurred or where potential failure exists. We suggest that hydrothermal activity (alteration and pore pressure effects) plays a significant role in collapse generation for two reasons: (1) it creates weak zones in the edifice where failure can occur when phenomena like magma intrusion or seismic events occur. This concerns, for example, the Mt St Helens and Soufriere Hills cases cited above. (2) It induces gravitational deformation of the edifice and subsequent flank destabilization as shown in the experiments.

Flank bulging is one of the features developed during gravitational deformation of altered core volcanoes. A similar bulge can also be produced by magma intrusion (Donnadieu and Merle 1998; Donnadieu et al. 2003). Distinction between these two phenomena that produce similar features can be done using quantitative information obtained in the laboratory for each deformation. This can be achieved using digital photogrammetry and profile displacements based on series of images. Compared to ductile core models, intrusion models present: (1) a larger horizontal component in the bulge area, (2) a possible continuous and positive Z deformation for some points on the bulge, (3) a global positive volume balance and (4) a more rapid deformation.

Conclusions

Hydrothermal system activity produces, through rock alteration and high pore pressure, a weak zone inside a volcano. The altered volcano core deforms under gravity. Our analogue modelling has characterised this phenomenon. The models show:

- A characteristic concave-convex-concave profile of deformed flanks. Two deformation patterns exist depending on whether the altered core is centred or not relative to the edifice. The symmetric case is characterized by an extension area of variable size in the upper part of the cone with radial and concentric normal faults, and small thrusts at the foot of the convex area (bulge belt). In an asymmetric configuration, preferential spreading occurs. Sub-vertical crescent faults develop at the slump summit and thrusts appear at its front. Normal faults orthogonal to the deformation axis appear on the slump sector and sometimes grabens develop on the summit.
- Deformation is controlled by the volume, the position and the dimensions of the ductile core relative to the edifice size. The volcano can deform even if only a small fraction of the rock is altered: 10% of the total edifice volume is sufficient.
- Vertical displacement dominates in the upper part of the cone, while maximum horizontal displacement appears at the upper concave-convex transition and in the bulge area.
- It is a long-term deformation that takes tens to thousands of years, taking into account the appropriate scaling and viscosities.
- Preferential spreading is the most frequent case as perfect symmetry does not really exist in nature, or in the laboratory. The resulting flank destabilization constitutes a major risk for these volcanoes. Small to huge catastrophic flank collapses can potentially occur, even if the volcano is dormant and thus not well monitored. Particular attention needs to be paid to volcanoes presenting such suspicious features, and suitable monitoring programmes are necessary to deal with the potential hazards.

We have outlined similar deformation patterns on several volcanoes, confirming that these phenomena exist in nature. This leads to questions regarding the common horseshoe structure on volcanoes. It is of interest to re-examine such structures that have previously been interpreted as collapse scars, because they could also be induced by flank spreading and thus be a pre- rather than a post-collapse feature.

Acknowledgements We thank the two reviewers, Lionel Wilson and Bill McGuire, for their valuable comments. The research was supported through the CNRS/INSU (French PNRN and ACI-CATNAT programmes).

References

Alidibirov M, Dingwell DB, Stevenson RJ, Hess KU, Webb SL and Zinke J (1997) Physical properties of the 1980 Mount St Helens cryptodome magma. Bulletin of Volcanology 59: 103–111

Alvarado GE (2000) Volcanes de Costa Rica. pp 283

Alvarado GE (2003) Diagnóstico de la estabilidad del cono y comportamiento de la fundación debido al crecimiento del edificio volcánico del Arenal (Costa Rica). MSc Thesis, Universidad de Costa Rica, San José

Alvarado GE and Leandro C (1999) Geological-geophysical study of an eastern and western section in the Arenal volcano. Bol. OSIVAM 20–21:48–58

Borgia A and Linneman SR (1990) On the Mechanisms of Lava Flow Emplacement and Volcano Growth: Arenal, Costa Rica. Lava flows and domes emplacement; mechanisms and hazard implications. F. J. H. Berlin, Germany, Springer Verlag: pp 208–243

Borgia A, Ferrari L, Pasquarè G (1992) Importance of Gravitational spreading in the tectonic and volcanic evolution of Mt. Etna. Nature 357:231–235

Borgia A Lanari R, Sansosti E, Tesauro M, Bernadino P, Fornaro G, Neri M, Murray JB (2000) Actively growing anticlines beneath Catania from the distal motion of Mount Etna's decollement measured by SAR interferometry and GPS. Geophys Res Lett 27:3409–3412

Cecchi E, van Wyk de Vries B and Lavest JM (2003) N-view reconstruction: a new method for morphological modelling and deformation measurement in volcanology. Journal of Volcanology and Geothermal Research 123:181 - 201

Claudin P (1999) La physique des tas de sable; Description phénoménologique de la propagation des contraintes dans les matériaux granulaires. pp 241

Cobbold PR and Castro (1999) Fluid pressure and effective stress in sandbox models. Tectonophysics 301((1–2)): 1–19

Day S (1996) Hydrothermal pore fluid pressure and the stability of porous, permeable volcanoes. Volcano instability on the Earth and Other Planets. W. J. McGuire, Jones, A.P. & Newberg, J., Geological Society Special Publication. 110: pp 77–93

Donnadieu F, Keelson F, van Wyk de Vries B, Cecchi E and Merle O (2003) Digital photogrammetry as a toll in analogue modelling: applications to volcano instability. Journal of Volcanology and Geothermal Research 123:161–180

Donnadieu F and Merle O (1998) Experiments on the indentation process during cryptodome intrusion: new insights into Mt St Helens deformation. Geology 26:79–82

Fournier (1999) Hydrothermal Processes Related to Movement of Fluid From Plastic into Brittle Rock in the Magmatic-Epithermal Environment. Economic Geology 94(8): 1193–1211

Froger JL, Merle O, Broiler P (2001) Active spreading and regional extension at Mount Etna imaged by SAR interferometry. Earth Planet Sci Lett 187:245–258

Garduño VH, Neri M, Pasquaré G, Borgia A, Tibaldi A. (1997) Geology of the NE rift of Mount Etna, Sicily (Italy). Acta Vulcanol 9:91–100

Girard G (2002) Relations volcano-tectoniques entre le complexe volcanique Las Sierras-Masaya et le graben de Managua, Nicaragua. Clermont-Ferrand, Université Blaise Pascal. pp 50

Hazlet RH (1987) Geology of San Cristobal volcanic complex, Nicaragua. Journal of Volcanology and Geothermal Research 33:233–240

Hubbert MK (1937) Theory of scale models as applies to the study of geologic structures. Geol. Soc. Am. Bull. (48): 1459–1520

Kerle N, van Wyk de Vries B (2001) The 1998 debris avalanche at Casita volcano, Nicaragua – investigation of structural deformation as the cause of slope instability using remote sensing. J Volcanol Geotherm Res 105: 49–63

Komorowski JC, Norton G, Boudon G, Voight B, Watts R, Young S, Sparks S, Herd R and Walker C (1999) The 1997 flank-collapse of Soufriere Hills, Montserrat: Constraints on emplacement mechanisms from debris avalanche. Morphological and textural data. Eos Trans. AGU Fall Meeting, San Francisco

Lopez D and Williams SN (1993) Catastrophic volcanic collapse: relation to hydrothermal alteration. Science 260(5115): 1794–1796

Merle O and Borgia A (1996) Scaled experiments of volcanic spreading. Journal of Geophysical Research 101(B6): 13,805–13,817

Merle O and Lénat J-F (2003) Hybrid collapse mechanism at Piton de la Fournaise (Reunion Island, Indian Ocean). Journal of Geophysical Research (in press)

Merle O and Vendeville B (1995) Experimental modelling of thin-skinned shortening around magmatic intrusions. Bulletin of Volcanology 57:33–43

Murray JB, Voight B and Glot JP (1994) Slope movement crisis on the east flank of Mt Etna volcano: Models for eruption triggering and forecasting. Engineering Geology 38:245–259

Petley DN (1996) The mechanics and Landforms of Deep-seated Landslides. Advances in Hillslope Processes

Petley DN and Allison RJ (1997) The mechanics of deep-seated landslides. Earth Surface Processes and Landforms 22:747–758

Ramberg H (1981) Gravity deformation and the Earth's crust. Academic Press, San Diego, California, pp 452

Siebert L (1984) Large volcanic debris avalanches : characteristics of source areas, deposits, and associated eruptions. Journal of Volcanology and Geothermal Research 22:163–197

Siebert L, Glicken H and Ui T (1987) Volcanic hazards from Bezymianny- and Bandaï-type eruptions. Bulletin of Volcanology 49:435–459

Swanson D, Hausback BP and Zimbelman DR (1995) Why was the 1980 bulge on the north flank of Mount St Helens? IUGGXXI Assembly (Int. Un. Geodesy Geophysics)

Vallance KM, Kerle JW, Macias JL, Strauch W and Devoli G (2003) Catastrophic precipitation-triggered lahar at Casita volcano, Nicaragua—Flow bulking and transformation. Bull. Geol. Soc. Am (in press)

van Wyk de Vries B and Francis PW (1997) Catastrophic collapse at stratovolcanoes induced by gradual volcano spreading. Nature 387:387–390

van Wyk de Vries B, Kerle N and Petley D (2000) A sector collapse forming at Casita volcano, Nicaragua. Geology 28(2): 167–170

van Wyk de Vries B and Matela R (1998) Styles of volcano-induced deformation: numerical models of substratum flexure, spreading and extrusion. Journal of Volcanology and Geothermal Research 81:1 - 18

van Wyk de Vries B and Merle O (1998) Extensional structures induced by volcanic loading in strike-slip fault zones. Geology 26:983–986

Voight B, Ed. (1979) Rockslides and avalanches. Amsterdam, Elsevier pp 752

Voight B and Elsworth D (1997) Failure of volcano slopes. Géotechnique 47: 1–37

Wallace LK and Waythomas CF (1999) Geologic setting and characterization of a large volcanic debris avalanche deposit in the Copper River Basin, Alaska. Eos Trans. AGU Fall Meeting, San Francisco

Wohletz K and Heiken G (1992) Volcanology and geothermal energy. pp 432